

# Automated Identification of Stereoelectroencephalography Contacts and Measurement of Factors Influencing Accuracy of Frame Stereotaxy

Radek Janca, Martin Tomasek, Adam Kalina, Petr Marusic, Pavel Krsek, Robert Lesko

**Abstract— Objective:** Stereoelectroencephalography (SEEG) is an established invasive diagnostic technique for use in patients with drug-resistant focal epilepsy evaluated before resective epilepsy surgery. The factors that influence the accuracy of electrode implantation are not fully understood. Adequate accuracy prevents the risk of major surgery complications. Precise knowledge of the anatomical positions of individual electrode contacts is crucial for the interpretation of SEEG recordings and subsequent surgery. **Methods:** We developed an image processing pipeline to localize implanted electrodes and detect individual contact positions using computed tomography (CT), as a substitute for time-consuming manual labeling. The algorithm automates measurement of parameters of the electrodes implanted in skulls (bone thickness, implantation angle and depth) for use in modeling predictive factors influencing implantation accuracy. **Results:** Fifty-four patients evaluated by SEEG were analyzed. A total of 662 SEEG electrodes with 8,745 contacts were stereotactically inserted. The automated detector localized all contacts with better accuracy than manual labeling ( $p < 0.001$ ). The retrospective implantation accuracy of the target point was  $2.4 \pm 1.1$  mm. A multifactorial analysis determined that almost 58% of the total error was attributable to measurable factors. The remaining 42% was attributable to random error. **Conclusion:** Designed algorithm reliable detected and measured SEEG electrodes thereby allowed assessment implantation accuracy of used frame-stereotaxy, and revealed factors to predict implantation accuracy. **Significance:** The novel automated image processing is a potentially clinically important assistive tool for increasing the yield, efficiency, and safety of epilepsy.

This study was supported by Ministry of Education Youth and Sports of the Czech Republic – Research Center for Informatics (CZ.02.1.01/0.0/0.0/16019/00000765) and grants of the Ministry of Health of the Czech Republic (NV19-04-00369, NU21J-08-00081).

Radek Janca (Corresponding author) is with the Department of Circuit Theory, Faculty of Electrical Engineering, Czech Technical University in Prague, Prague, Czech Republic (e-mail: janca.radek@fel.cvut.cz).

Martin Tomasek and Robert Lesko (Senior author) are with Department of Neurosurgery (e-mail: martin.tomasek@fnmotol.cz, and robert.lesko@fnmotol.cz). Adam Kalina and Petr Marusic are with Department of Neurology (e-mail: adam.kalina@fnmotol.cz, and petr.marusic@fnmotol.cz), and Pavel Krsek is with Department of Paediatric Neurology (e-mail: pavel.krsek@fnmotol.cz), Second Faculty of Medicine, Charles University and Motol University Hospital, Prague, Czech Republic.

The authors are members of the Epilepsy Research Centre Prague - EpiReC consortium and Motol University Hospital is a member of ERN EpiCARE.

surgery planning and treatment.

**Index Terms—** bone thickness, Cosman–Robert–Wells, epilepsy surgery, image processing, implantation angle

## I. INTRODUCTION

RESECTIVE epilepsy surgery is an established and effective therapeutic method in the treatment of patients with intractable focal epilepsy, with an expected effectiveness of up to 80% [1]–[3]. Complete removal of the epileptogenic zone with preservation of the eloquent brain structures is essential for the most desirable outcome of the surgery – a seizure-free patient without a new neurological deficit [4], [5]. To achieve this goal, it is necessary to define the boundaries of the epileptogenic zone and eloquent cortical areas precisely. In cases with a good correlation of seizure semiology and both electrophysiology and neuroimaging findings, an excellent surgery outcome can be expected based on these non-invasive examinations only. Otherwise, if a strong localization hypothesis is needed for verification or if lesion delineation has to be specified, an invasive protocol is available using the intracranial electrophysiological method [4], [6]–[8].

Invasive intracranial EEG (iEEG) can be performed using either subdural strips and grids or stereotactically inserted electrodes (SEEG). The stereotactic method is not only more efficient than the subdural implantation technique, mainly because of the availability of deep structures, but also safer [9]–[11]. In addition to SEEG, frame stereotaxy is used for the insertion of deep brain stimulation electrodes (DBS), as well as for thin-needle biopsies of deep-seated tumors. The spectrum of epilepsy surgery candidates significantly changes together with increasing case complexity. Candidate patients can benefit from surgery treatment that would not previously have been considered for them. The importance of invasive methods, especially SEEG, is increasing despite advances in non-invasive neuroimaging methods [12], [13]. This trend is observable not only in Europe, where stereotaxy has been an important modality for a long time, but also in the United States, where subdural implantations have dominated in the past [14], [15].

Adequate stereotaxic accuracy prevents the risk of the most feared complication: bleeding from vascular injury due to

inaccurate electrode insertion. Precise electrode placement also increases the yield of monitoring epileptic activity and allows mapping of eloquent areas, both of which are primary goals of implantation. The accuracy of deep electrode implantation, regardless of the indication (DBS or SEEG), has been evaluated in previous research mainly by comparing the actual position of the electrode tip to its planned position [16], [17]. However, knowledge of all electrode contact positions is crucial for SEEG because it is essential to know the anatomical origin of the epileptogenic activity.

Therefore, contacts in the middle of the electrode can play a more important role than those near the electrode tip. Individual contacts can be labeled manually, although this is extremely time-consuming and demands close attention and great experience with electrode imagination in a three-dimensional (3D) space. Efforts have been made to develop semi-automated/automated detection methods [18]–[22]. In addition, the visibility of some contacts can be almost impossible to distinguish from metal artifacts in computed tomography (CT) which involves many crossing electrodes.

The ultimate implantation accuracy achieved can be influenced by many factors arising from interference of electrode trajectories with the individual patient's anatomy [23], [24] and these risky situations are difficult to assess visually. The need for a reliable automated detector and algorithm for morphological measurement in medical images is increasing as the number of implanted electrodes increases, with hundreds of contacts per patient.

The goals of this study were the following: 1) to develop an algorithm for automated detection of contacts of stereotactically inserted deep SEEG electrodes and verify the reliability, time efficiency, and accuracy of this algorithm; 2) to develop an image-measuring algorithm for recognizing potentially risky electrodes from the perspective of bone thickness and implantation angle; and 3) to evaluate the accuracy of implantation in our cohort and identify variables that affect this accuracy using the proposed methodology.

## II. MATERIALS AND METHODS

### A. Clinical data, patients, and data selection

We retrospectively analyzed 51 patients who underwent 54 SEEG explorations followed by iEEG monitoring as part of an evaluation before resective epilepsy surgery at Motol Epilepsy Center in Prague between 2015 and 2021. Data collection was approved by the Ethics Committees for Multicentric Clinical Trials of the University Hospital Motol and 2nd Faculty of Medicine, Charles University in Prague and informed consent was obtained. A total of 662 SEEG electrodes (8,745 contacts; Dixi Médical, France) were implanted using a Cosman–Robert–Wells (CRW) stereotactic frame system (CRW Precision<sup>TM</sup> Integra Lifesciences, USA).

Magnetic resonance imaging scans conducted under an epilepsy protocol (<1 mm high-resolution isotropic T1- and T2-weighted) were obtained for diagnosis and subsequent planning of electrode placement. The stereotactic frame was fixed to a patient using a local anesthetic and four self-penetrating screws, which create an immobile and stable platform. Pre-surgery CT ( $\leq 1 \times 1 \times 0.5$  mm) was conducted using

a Luminant® MR/CT localizer (CT-L; Integra<sup>TM</sup>, USA), which defines the rectangular coordinate space of the stereotaxy. The StealthStation Surgical Navigation planning system (ver. S7 or S8, Medtronic, USA) was used to co-register CT-L to magnetic resonance images (MRIs) and compute operation adjustments of the frame (three translations, two angles, orientation) for all electrodes, based on trajectory planning. The patient's head was fixed using the frame to the surgery table, together with a removable arc. A phantom construction validated each trajectory setting before skull drilling, anchor bolt screwing, and dura mater penetration. Electrodes were inserted at the end of the surgery. The post-implantation CT with electrodes (CT-E) in the naturally blurred soft tissue window was co-registered with MRI to show the final electrode position immediately after surgery. Each contact was marked manually by an experienced clinical engineer using the BioImage Suite 3.0 software in Electrode Editor [22]; see details in section II-G. The coordinates were exported from the image coordinate system (IJK) to the anatomical coordinate system in RAS (left→right, posterior→anterior, inferior→superior) that allowed rapid navigation in 3D slice viewer – 3D Slicer [25]. Manual labeling defined gold-standard references for validation of the automated detection.

### B. Rectangular template of CT with localizer

The Luminant® MR/CT localizer represents a rectangular referential space and fiducials for CRW to which electrode trajectories are related. The pre-surgery CT-L adopts the scanner coordinate space, which had to be transformed to the referential space using the planning software. However, this system is closed to the user. Consequently, we had to create our trustworthy image template of the localizer (Fig. 1A). The initial template models orthogonal luminant tubes to an orthogonal cage based on the technical specifications of the producer at 0.5-mm isotropic resolution. We predicted the co-registration failure between the simple cage model and the patient's CT-L due to the limited mutual information used in the SPM12 toolbox for MATLAB [26], [27]. Therefore, we iteratively aligned and added other CT-L scans to the emerging average template, which was used for initial CT-L realignment before fine registration of the cage model. Finally, all co-registered CT-L scans were resliced, averaged, and smoothed using a Gaussian filter (full width at half maximum,  $FWHM = 5$  mm), except the cage to the Luminant template (Fig. 1B-D).

### C. Image co-registration and pre-processing

The co-registration process found affine transformations between fixed and moving images, whereas MRI (T2) was a general reference. The whole co-registration pipeline is shown in Fig. 2. MRI images were segmented to obtain tissue maps (gray matter – GM, white matter – WM, cerebrospinal fluid – CSF) using SPM12 and were additionally resliced to CT-E for intracranial space masking.

Operation frame adjustments of electrode trajectories were recalculated to vector representation by the target-point  $TG = [TG_r; TG_a; TG_s]$  and directional vector

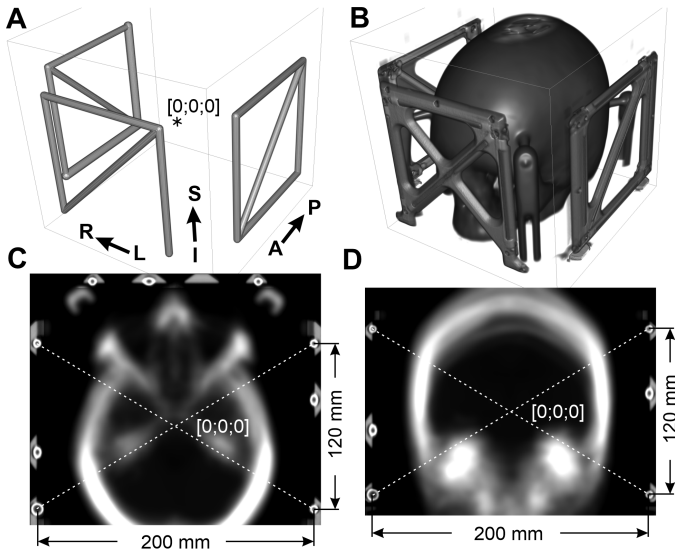


**Fig. 1.** Template of CT with Luminant localizer. (A) Rectangular model of referential Luminant tubes. (B) Resulting template of 54 co-registered and averaged CT-L scans. (C) Axial template slice with indicated zero point [0;0;0] of CRW space as an intersection of contralateral edges, (D) in coronal.

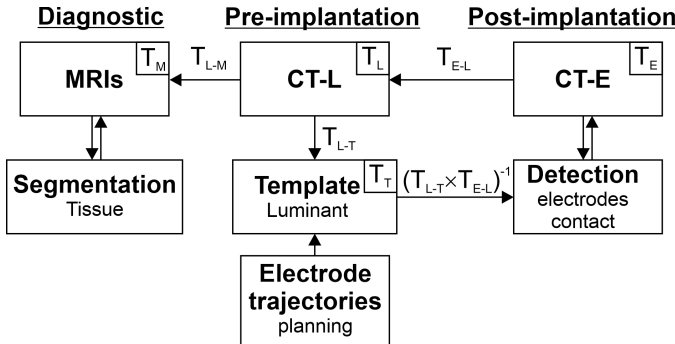


**Fig. 2.** Scheme of image co-registration pipeline. All images (MRI, pre-operative CT-L, pos-implant CT-E, Luminant template) were realigned to MRI. Mapping from voxel IJK space to spatial RAS defined directional affine transformations ( $T_M, T_L, T_T, T_E$ ) and mutual volumes realignment transformations (moving→fixed:  $T_{L-M}, T_{E-L}, T_{L-T}$ ). Planned electrode trajectories could be transformed from Luminant template to CT-E by the inverse way  $T_{T-E} = (T_{L-T} \times T_{E-L})^{-1}$  as initialization of the electrode detector. Combination of transformations allowed representation of any point between volumes and coordinate systems.

$\vec{V} = [V_r; V_a; V_s]$  in the Luminant template space;  $\{r, a, s\} \in \text{RAS}$ . Representation in the CT-E space was obtained by applying the realignment transformation from the Luminant template to CT-E:  $T_{T-E} = (T_{L-T} \times T_{E-L})^{-1}$ , where  $T_{L-T}$  is a transformation from CT-L to the Luminant template, and  $T_{E-L}$  is from CT-E to CT-L. The parameters of trajectories were used for the initialization of an automated electrode detector.

#### D. Detection of electrodes

The post-implantation CT-E contained metal electrodes, including x-ray artifacts, wires, and connectors, which complicated individual contact identification and localization. Therefore, CT-E was limited by  $\text{ROI}_H$  – the head region of interest.

The  $\text{ROI}_H$  was composed of MRI tissue (GM, WM, CSF, BONE) and CT solids (Hounsfield unit  $HU > -150$ ) merged to a mask, which was additionally morphological denoised (2-mm erosion, 6-mm dilatation, 10-mm erosion).

The positions of implanted electrodes are usually imprecise with respect to planned trajectories, slightly wavy, and sometimes curved [17], [23], [28] (Fig. 3A). Therefore, attributes of electrodes ( $\text{TG}, \vec{V}$ , label name, number of contacts) could not be correctly assigned to appropriate metal voxels (platinum,  $HU > 3000$  [18]). We used the Gaussian mixture model classifier (GMM) to identify voxel groups of straight electrodes. GMM was not initialized randomly but rather as a mix of elongated ellipsoids oriented in the planned electrodes trajectories (the minor semiaxis was 1% of the major semiaxis). The ellipsoid lay between the imaginary electrode tip ( $\text{TG}$ ) and the last contact ( $\text{TG} + L\vec{V}$ ), where  $L = 2N + 1.5(N - 1)$  is the length of the  $N$ -channel electrode, with a contact size of 2 mm and 1.5-mm space. The pattern to classify was the IJK coordinates of each metal voxel CT-E from  $\text{ROI}_H$ . If the patient had metal implants in the head volume (5 of 54 cases; e.g., shunt, clips, amalgam seal), CT-E was masked by metals thresholded from CT-L. The pre-initialized GMM fitted metal voxels to final clustering of individual electrodes as well, with parts of the anchor bolts under the skin ( $\text{ROI}_{EL}$  – a cluster) (Fig. 3B). Initial CT-E thresholding ( $HU > 3000$ ) could cause loss of voxels/contacts due to x-ray shadowing behind metal. Therefore, each  $\text{ROI}_{EL}$  was analyzed to find each electrode as series of coupled contacts (*electrode model*).

#### E. Automated contact localization

The diameter of the electrodes was only  $\varnothing 0.8$  mm, which was similar to or less than the CT resolution. A precise individual contact center could not be measured directly in voxel-raster but rather had to be estimated in naturally blurred CT-E. A polynomial function fitted voxels in appropriate  $\text{ROI}_{EL}$  independently for each electrode to obtain curved central axis of the electrode.

Fitting a curve in a 3D space is problematic in general. However, a physical electrode is usually isomorphic, and the task can be accomplished by superposition of two two-dimensional (2D) orthogonal projections with a maximal variance of  $\text{ROI}_{EL}$  voxels (X-Y, and X-Z) (Fig. 3C). Two third-order polynomials defined the fitted central axis  $y = P_{X-Y}(x)$ ,  $z = P_{X-Z}(x)$ , where  $x$ ,  $y$ , and  $z$  represent positions in the 2D projections. The fitting weights of the voxels corresponded to intensity in CT-E. The 3D curve obtained represented the central axis of the electrode from the tip up to the anchor bolt (i.e., the physical trajectory), which was subsequently used to trace contacts and measure the bone thickness and implantation (tangential) angle to the skull, as described in section II-F.

The contact was a 2-mm high cylinder with a 0.8-mm diameter, which was visualized as a blurred ball in CT-E. Therefore, its position defined the geometric center. The electrode model represented a series of coupled contacts (Gaussian balls  $\sigma = 0.8$  mm with 3.5-mm spacing) placed in the central axis that looked like a “coral necklace”; thus, contact tracing for each electrode was performed at once. The coupled balls

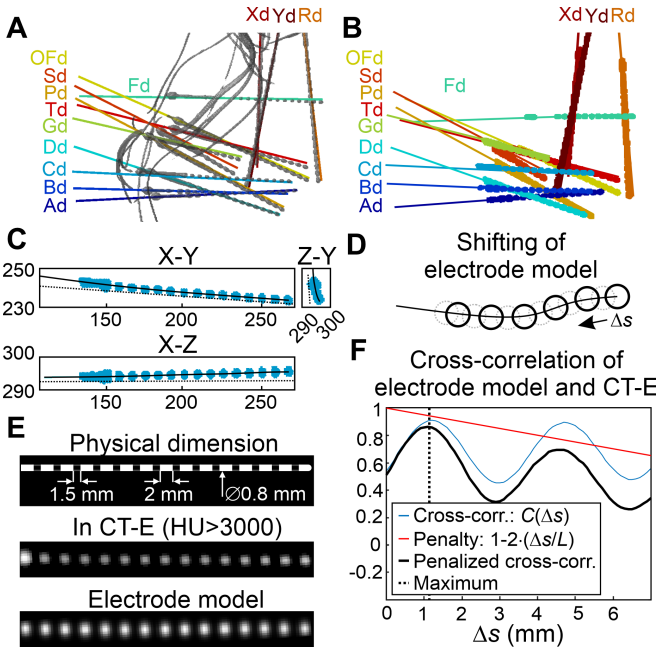


**Fig. 3.** Electrode identification and contact localization. (A) CT-E scan thresholded by  $HU > 3,000$  shows gray metal voxels. Colored trajectories of planned electrodes initialize the GMM algorithm. (B) Clustering of metal voxels to groups represents electrodes  $ROI_{EL}$ . (C) Metal voxels in  $ROI_{EL}$  (e.g., electrode “Cd”) are projected to two 2D planes by maximal variance in X-Y and X-Z. Voxels in planes are fitted by third-order polynomial approximations:  $y = P_{X-Y}(x)$ ,  $z = P_{X-Z}(x)$ , which defines the central axis of an electrode (black curve). A dotted line marks a planned trajectory. (D) The electrode model consists of serialized and coupled Gaussian balls with 3.5-mm spacing on a central axis. Balls are systematically shifted ( $\Delta s = 0.1$  mm). (E) After shift, rebuilding models are correlated with CT-E. (F) Maximum of cross-correlation function (blue)  $C(\Delta s)$  determines a match between CT-E and shifting model that defines coordinates of all contacts. A shift penalty (red line) is incorporated to protect the missing of the first, sometime ambiguous, contact.

were gradually shifted from the deepest metal voxel (tip) to the skull in steps  $\Delta s = 0.1$  mm. Shifting models were correlated with CT-E to find the best match, (Fig. 3D and E). The shift under image resolution was possible because of the continuous Gaussian probability density function that defined each ball in the voxel raster. The position of the maximum in the cross-correlation function  $C(\Delta s)$  obtained indicated the best electrode model with coordinates of Gaussian balls centers, i.e., final contact coordinates (Fig. 3F). However,  $C(\Delta s)$  was periodic with the contact spacing. Because artifacts around the electrode tip could sometimes cause incorrect positioning of the first contact as the second, the cross-correlation was penalized by the shift as follows:

$$C(\Delta s) \cdot [1 - 2(\Delta s/L)]. \quad (1)$$

The electrode tip position (TIP coordinates) was 1 mm before the first contact.

#### F. Bone measurement and entry point parametrization

The planned electrode entry points (ENT) were localized at the intersection of the planned trajectories with the extracranial edge of the skull bone. The drilling entry points (DENT) were

marked at the intersection of the skull and the electrode central axis. Precise localization of the bone edge in the entry was impossible in a CT-E. The bone was drilled out and filled by a metal anchor bolt, producing a metal artifact in the surrounding area in CT-E (Fig. 4A). Therefore, pre-surgery CT-L was used for bone measurement instead (Fig. 4B).

A voxel intensity along the electrode trajectory of  $HU > 300$  (cancellous bone) indicates skull (Fig. 4C). A gap between cortical bone sides could occur due to voids in spongy tissue. Therefore, morphological operations fill the gap (5-mm dilatation and erosion). Edges define coordinates of intracranial and extracranial entry points, and their distance  $\|B\|$  corresponds to the bone length (thickness) in the electrode trajectory.

The implantation angle between an electrode and an unevenly spherical skull is one of the essential parameters that can potentially influence the precision of initial drilling. Ideally, this angle should be  $90^\circ$ . Real electrodes are inserted with a recommended angle deviation  $\alpha < 30^\circ$  (implantation angle  $90^\circ - \alpha$ ). A surgeon can manually measure the angle only approximately during the planning process, as the minimal trajectory angle to the skull in the coronal, axial, or sagittal views. Therefore, we have implemented a precise method to measure a minimal implantation angle in 3D.

Based on the previously identified external entry point, a spherical 10 mm surrounding was extracted from CT-L as a segment of the skull around the electrode trajectory ( $ROI_{skull}$ ). A kernel of a directional gradient filter was designed as a “flat disc” ( $\varnothing 4$  mm) perpendicular to the electrode trajectory  $\vec{e}$ . Gradient filtering of  $ROI_{skull}$  highlighted the borderline of the skull surface, with voxels above half of the maximal gradient defining a surface canopy (Fig. 4D). The canopy fitted the plane whose normal vector  $\vec{n}$  represented the ideal implantation direction to the skull at the entry point ( $90^\circ$ ). The dot product  $\alpha = \text{acos}(\vec{n} \cdot \vec{e})$  computes the angle between the normal vector  $\vec{n}$  and the electrode trajectory  $\vec{e}$  that is complementary to finding the implantation angle ( $90^\circ - \alpha$ ). The implantation angle  $\alpha$  obtained is used to estimate the skull thickness at the entry point  $B_\perp = \|B\| \cdot \sin(90^\circ - \alpha)$ . The process described above was used to measure planned and detected electrode trajectory parameters. An anchor bolt direct trajectory  $\vec{e}_{bolt}$  was defined between intracranial and extracranial entry points.

#### G. Manual labeling as a reference for automated detection

Each referential contact position was obtained by manual/semi-automated labeling using the BioImage Suite 3.0 software in Electrode Editor [22]. The editor showed the thresholded CT-E that was visualized, and we were able to rotate a 3D image ( $x, y, z$ ) to a 2D screen projection ( $x, y$ ). The labeled contact was traced manually using the mouse cursor ( $x, y$ ), and the depth ( $z$ ) was determined by the best fit of a Gaussian ball (1, 5, or 10 mm) automatically. The correct fit had to be visually validated in all axes and manually edited if distorted because of x-ray artifacts, low resolution, etc. Contacts on the same SEEG electrode are grouped and

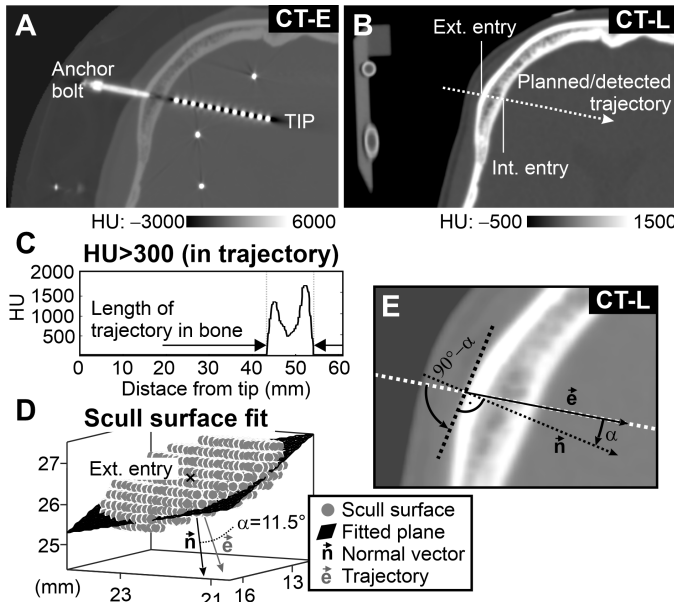


**Fig. 4.** Measurement of bone thickness and implantation angle of electrode trajectory with respect to skull surface. (A) Post-implantation CT-E shows electrode contacts and the metal anchor bolt that preserves precise localization of the external skull borderline. (B) The borderline of the skull is detected as an intersection of the detected/planned electrode trajectory (white dotted line) in pre-surgery CT-L. (C) Image intensity ( $HU > 300$ ) along the trajectory localizes bone tissue. Edges determine intracranial and extracranial entry points. (D) The tangent plane of the spherical skull surface fits the extracranial skull canopy around the entry point. The angle between the normal vector of plane  $\vec{n}$  and the electrode trajectory  $\vec{e}$  defines the deviation  $\alpha$  from the right angle of the plane. The implantation angle is thus  $90^\circ - \alpha$ . (E) Detail of CT-L shows vectors ( $\vec{n}$  and  $\vec{e}$ ) and angle ( $\alpha$ ) in axial view.

named by letter prefix and numeric order from the tip contact. Manual labeling marked less than half of the contacts (every second or third contacts), and skipped contacts were linearly positioned between the marked contacts using the editor warping function. The final coordinates were stored in IJK space and transformed to RAS of MRI. The whole process is time-consuming, requiring up to an hour for an expert to complete, depending on the number of electrodes implanted, the clarity of the electrode placement, and reader imagination in assigning the right electrode to metal voxels. The labeling process was performed on the date of the implantation.

The minimal Euclidian distance defines the pair match/mismatch between manually labeled contacts and automated detections. The quality of homogenous contact displacement was expressed in terms of the variance in contact spacing (physical spacing 3.5 mm) and the deviation from the central electrode axis (Fig. 5). The central axis deviation measures the distance of the middle contact from the line connecting its neighbors. The remaining variance caused by the curvature of electrodes was ignored.

### III. RESULTS

#### A. Automated localization of electrode contacts

The CT and MRI images from 54 implantations of 662 SEEG electrodes with 8,745 contacts were processed automatically and compared with manual labeling. On average,

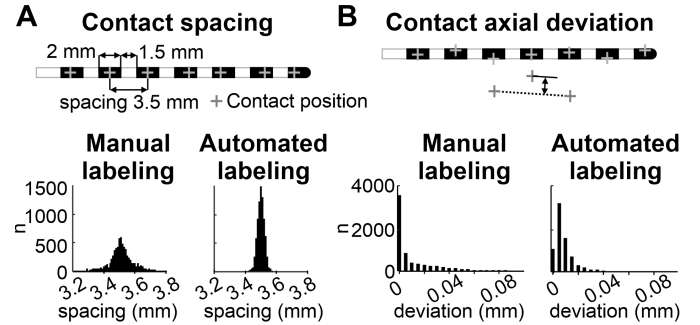


**Fig. 5.** Comparison of contact position homogeneity between manual and automated labeling. (A) Contact spacing is measured as the Euclidian distance between neighboring contacts, ideally 3.5 mm of physical contact spacing. Manual labeling shows significantly higher variability ( $\pm 0.126$  mm) than automated labeling ( $\pm 0.023$  mm) ( $p < 0.001$ ; Ansari–Bradley test), whose variance was caused by only curvature of the electrode. (B) A contact's axial deviation is defined as the distance from the line between two neighboring contacts. The most frequent zero deviation in manual labeling reflected linear displacement of contacts by the electrode editor warping function. The total variance was lower for automated labeling ( $0.01 \pm 0.016$  mm,  $IQR = 0.008$  mm) than for manual labeling ( $0.021 \pm 0.024$  mm,  $IQR = 0.024$  mm) ( $p < 0.001$ ; Ansari–Bradley test), and non-zero deviations corresponded better to the curving of electrodes.

$12.3 \pm 3.6$  electrodes (median 12, minimum 4, maximum 19) with  $162 \pm 52$  contacts (median 154.5, minimum 54, maximum 288) were implanted per patient. Automated detection of electrodes, as described in section II-D, correctly identified and named all of the electrodes (662 of 662). Crossing and touching electrodes were also correctly separated by the GMM algorithm for the localization of individual contacts.

Subsequent automated contact localization (II-E) initially failed for 8 of 662 electrodes due to skipping of the first contacts (at the tip), and the remaining contacts of the electrode were therefore shifted by one. Visual inspection of the failures revealed a scenario wherein the tip touched another electrode and distorted the first contact ball shape and intensity. Therefore, the correlation between the electrode model and the CT-E was higher for the model shifted to the second contact (second peak of cross-correlation; Fig. 3F). The added penalty function (1) resolved failures for all but one of the electrodes (661 of 662). In the one unresolved case, the first touching contact was almost unrecognizable visually in low-resolution CT-E ( $1 \times 1 \times 0.5$  mm), and its confirmation was based on counting and extrapolating of the remaining contacts. Therefore, the model shift  $\Delta s$  was manually set to the first peak in the cross-correlation. The total success rate of the automated labeling was 99.85%, increasing to 100% after manual correction for one electrode.

The average distance error [19] between the manually and automatically localized contacts was  $0.43 \pm 0.84$  mm (median 0.24 mm) under CT-E voxel resolution. Variability in the contact spacing (Fig. 5A) was lower for automated detection ( $\pm 0.023$  mm) in comparison to manual labeling ( $\pm 0.126$  mm) ( $p \ll 0.001$ ; Ansari–Bradley test). Similarly, the axial deviation was smaller for automated detection ( $IQR = 0.008$  mm) than for manual labeling ( $IQR = 0.024$  mm) ( $p \ll 0.001$ ; Ansari–Bradley test) (Fig. 5B).

**TABLE I**  
MEASUREMENT OF IMPLANTED ELECTRODES

Parameters	mean $\pm$ s.d.	med.	outliers	min.	max.
Bone thickness (mm)	6.6 $\pm$ 2.8	6.3	1.3%	1.3	19.1
Implantation angle ( $^{\circ}$ )	67.8 $\pm$ 9.8	68	0.34%	41.3	89.9
Electrode warping (mm)	0.4 $\pm$ 0.3	0.3	2.85%	0	12.3
Insertion depth (mm)	43.4 $\pm$ 13.4	43.3	2.18%	14.4	95.6
Plan vs. implantation error:					
Entry point (mm)	1.7 $\pm$ 1	1.6	2.85%	0.2	6.1
Target point (mm) <sup>1</sup>	2.4 $\pm$ 1.1	2.3	0.84%	0.2	7.5
1 <sup>st</sup> contact deviation (mm)	2.2 $\pm$ 1.1	2.1	1.01%	0.1	6.0
Insertion depth (mm)	0.5 $\pm$ 1.3	0.3	2.35%	-4.1*	8.3
Contact deviation (mm)	1.8 $\pm$ 1	1.7	0.87%	0	6
Trajectory deflection ( $^{\circ}$ )	1.8 $\pm$ 1.1	1.6	2.85%	0.1	12.6

Abbreviations: s.d. – standard deviation, med. – median, min. – minimum, max. – maximum. A negative value (\*) indicates that the insertion depth was exceeded.

### B. Skull bone measurement

The average implantation angle of the SEEG electrode trajectory with respect to the skull surface ( $90^{\circ} - \alpha$ ) was  $67.8^{\circ} \pm 9.7^{\circ}$  (median  $68.1^{\circ}$ ). However, 19.5% of the electrodes were implanted at angles of less than  $60^{\circ}$ , impairing the total implantation accuracy [24]. The lowest angle measurements were confirmed manually using 3D Slicer (see Fig. 6A).

The average bone thickness was  $B_{\perp} = 6.6 \pm 2.8$  mm (median 6.3 mm, minimum 1.3 mm, maximum 19.1 mm). Only 1.4% of the electrodes were fixed to the bone at less than the recommended minimum thickness of 2 mm. Outliers were remeasured and visually confirmed in 3D Slicer. The thicknesses at all entry points were visualized, extrapolated, and mapped to the surface of the SPM skull template (Fig. 6B and C). All measured parameters are summarized in Table I.

### C. Accuracy of electrode implantation

Visual comparison of the trajectories and implanted electrodes revealed one case in which the head ring (Universal Compact Head Ring Assembly, UCHRA) was shifted, probably due to loosening while the patient was being transported. The implantation scheme was modified in two cases, but without data backup. Therefore, these 3 of the 54 cases were excluded from the accuracy study (45 of 662 electrodes). The implantation failed for 21 of 617 (3.4%) electrodes because of unpredictable deformation after leaving the stylet's prepared track ( $n = 13$ ) and the inability to achieve the planned insertion depth ( $n = 8$ ) because of crossing with another electrode or higher mechanical resistance during insertion. These electrodes, characterized by  $TG_{ERR} > 6$  mm, were also excluded from the accuracy study.

The analysis of the implantation accuracy of the remaining 596 electrodes revealed three crucial parameters measured between the planned trajectories of the CRW adjustment and the physical positions of electrodes in CT-E: 1) target point error, 2) electrode entry point error, and angle deviation from the planned trajectory.

**1) Target point error:** The average target point error<sup>1</sup>  $TG_{ERR} = \|\mathbf{TG} - \mathbf{TIP}\|$  was  $2.4 \pm 1.1$  mm (median 2.3 mm). The  $TG_{ERR}$  consisted of two components: deviation from the planned trajectory and inaccurate electrode insertion depth. The planned insertion depth  $I = \|\mathbf{ENT} - \mathbf{TG}\|$  ( $43.4 \pm 13.4$  mm, median 43.3 mm) was partly affected by mechanical electrode warping after placement. Maximal measured contact warping from the electrode central axis was  $0.4 \pm 0.3$  mm (median 0.3 mm). A comparison of physical and planned insertion depths, defined as the distance between the external entry point and the tip,  $I_{ERR} = \|\mathbf{ENT} - \mathbf{TG}\| - \|\mathbf{DENT} - \mathbf{TIP}\|$ , revealed an average error of  $0.5 \pm 1.3$  mm (median 0.3 mm).

However, a more significant part of  $TG_{ERR}$  is represented by deviation from the planned trajectory,  $2.2 \pm 1.1$  mm (median 2.1 mm), i.e., the perpendicular distance from the first contact to the planned trajectory  $\vec{e}$  (Fig. 6D–F).

The  $TG_{ERR}$  in years 2015–2021 exhibited accuracy improvement by  $0.12 \pm 0.03$  mm per year (linear regression model,  $p < 0.001$ ) (Fig. 6G). The results are summarized in Table I.

**2) Entry point error and angle deviation:** The initial imprecision of drilling and anchor bolt positioning determined the entry point error  $ENT_{ERR} = \|\mathbf{ENT} - \mathbf{DENT}\|$ , on average  $1.7 \pm 1$  mm (median 1.6 mm). The electrode inherited this error as an offset on the tip and increased  $TG_{ERR}$ . The non-infinite rigidity of the CRW stereotaxy led to the angular deflection from the planned trajectory  $\vec{e}_{ERR} = \angle(\vec{e}, \vec{e}_{bolt})$ , on average  $1.8 \pm 1.1$  (median 1.6) degrees. Angular deflection added an average offset to contact position  $0.014 \pm 0.023$  mm per 1 mm of implantation depth, Fig. 6E.

### D. Multifactorial analysis

Measured parameters were evaluated together with the electrode implantation order, which could reveal a temporal progression of error during surgery. The Spearman coefficient was used to examine correlations among parameters and thereby identify effects influencing the target point error  $TG_{ERR}$ . The highest correlation ( $C = 0.52$ ,  $p < 0.001$ ) was with the entry point error  $ENT_{ERR}$ , followed by the angle deflection  $\vec{e}_{ERR}$  from the planned trajectory ( $C = 0.26$ ,  $p < 0.001$ ), insertion depth error  $I_{ERR}$  ( $C = 0.16$ ,  $p < 0.001$ ), and the bone thickness  $B_{\perp}$  ( $C = 0.11$ ,  $p < 0.01$ ). The direct effect of drilling at a low implantation angle ( $90^{\circ} - \alpha$ ) on implantation accuracy was minimal ( $C = -0.09$ ,  $p < 0.05$ ). The negative correlation ( $C = -0.27$ ,  $p < 0.001$ ) between the implantation angle and bone thickness reflects more perpendicular implantation of temporal structures for naturally thinner bone. The correlation of bone thickness with entry point error ( $C = 0.19$ ,  $p < 0.001$ ) reflects more difficult drilling control from the superior oblique direction [23]. Similarly, long electrodes (frontal, insular) usually entered under a low implantation angle ( $C = -0.20$ ,  $p < 0.001$ ) through thick bone ( $C = 0.12$ ,  $p < 0.001$ ). The entry point shifting over inhomogeneous bone thickness

<sup>1</sup>Target point error was also calculated for deformed/failed electrode implantation ( $n = 617$ ) for comparison with [23]:  $TG_{ERR} = 2.65 \pm 1.77$  mm (median 2.35 mm).

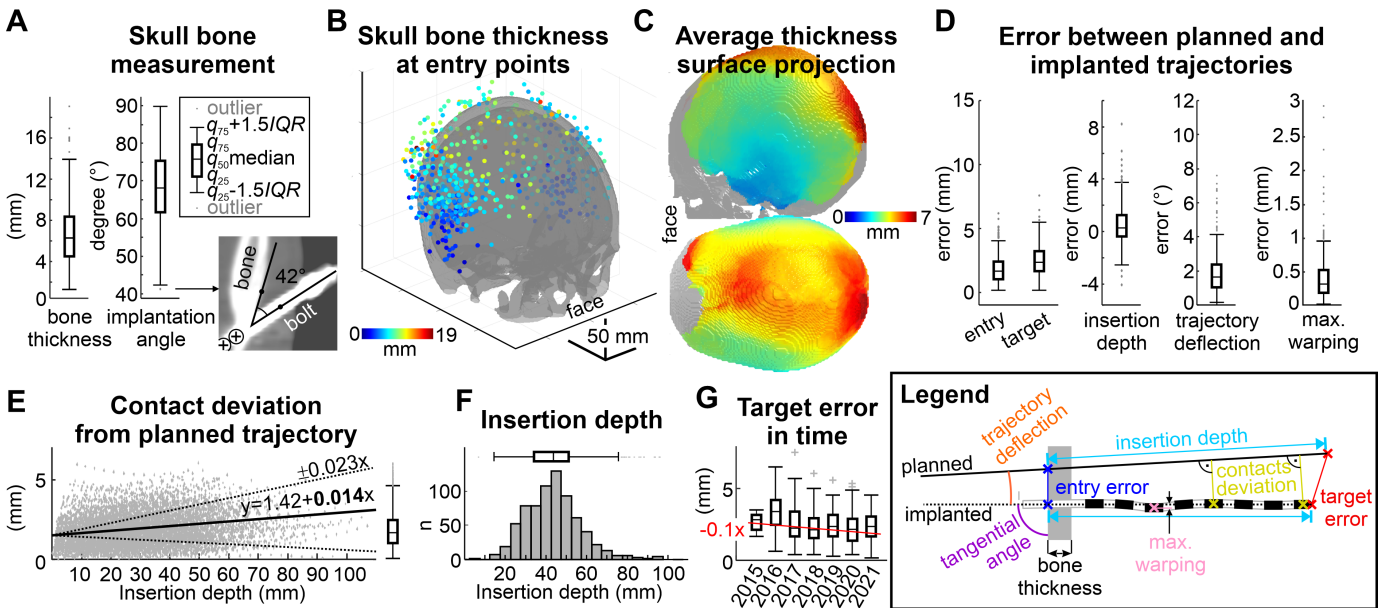


**Fig. 6.** (A) Average measured implantation angle of the electrode with respect to skull surface was  $67.8^\circ \pm 9.7^\circ$  (median  $68.1^\circ$ ). Intracranial and extracranial entry point distances were recalculated to bone thickness  $6.6 \pm 2.8$  mm (median  $6.3$  mm) on average. The lowest angles were visually validated; manual overviewing is shown for the outlier. (B) Bone thicknesses over the MNI template of the skull are indicated by the colored entry points and spatial extrapolation in (C). (D) The boxplots show the differences between planned and implanted electrode trajectories. The average error in the entry point  $ENT_{ERR}$  was  $1.9 \pm 1.3$  mm (median  $1.7$  mm) and  $2.8 \pm 1.9$  mm (median  $2.4$  mm) with respect to the target point  $TG_{ERR}$ . The total target point error is the result of imprecise electrode insertion depth  $I_{ERR} = 0.6 \pm 2$  mm (median  $0.3$  mm) and trajectory deflection error (measured at the bolt)  $\bar{e}_{ERR} = 1.8^\circ \pm 1.2^\circ$  (median  $1.7^\circ$ ). The implanted electrode warping is shown as the maximum axial distance of contacts from a straight trajectory of implanted electrodes:  $0.4 \pm 0.6$  mm (median  $0.3$  mm). (E) Each contact deviation from the planned trajectory depends on the depth position. (F) The distribution of electrode insertion depths was measured as the distance between the entry point and the tip. (G) The evolution of target point error observed in years 2015–2021 shows accuracy improvement by  $0.12 \pm 0.03$  mm per year.

causes insertion depth error that is correlated with entry point error ( $C = 0.24$ ,  $p < 0.001$ ), bone thickness ( $C = 0.11$ ,  $p < 0.01$ ), and negatively correlated with the implantation angle ( $C = -0.27$ ,  $p < 0.001$ ). The false discovery rate (FDR) method corrected all effects of multiple comparisons (Fig. 7A).

Generalized linear modeling by *stepwise* regression (GLM) extracted and estimated multifactorial predictors of the  $TG_{ERR}$ . The first model confirmed the correlation analysis results, combining the entry point error  $ENT_{ERR}$ , trajectory deflection  $\bar{e}_{ERR}$ , insertion depth  $I$ , and insertion error  $I_{ERR}$  in the following model:  $TG_{ERR} = 0.79 + 0.53 \cdot ENT_{ERR} + 12.75 \cdot \bar{e}_{ERR} + 0.007 \cdot I + 0.1 \cdot I_{ERR}$ . The estimated dispersion was  $0.908$  mm, and the F-statistic vs. the constant model was  $68.3$  ( $p \ll 0.001$ ). The trajectory deflection and insertion depth were merged into one parameter  $I \cdot \tan(\bar{e}_{ERR})$  for a more straightforward interpretation, with the distance deviation increasing with depth. The second, simpler, model was  $TG_{ERR} = 1.06 + 0.54 \cdot ENT_{ERR} + 0.31 \cdot I \cdot \tan(\bar{e}_{ERR}) + 0.09 \cdot I_{ERR}$ . The estimated dispersion was  $0.903$  mm, and the F-statistic vs. the constant model was  $92.2$  ( $p \ll 0.001$ ) (Fig. 7B). The models show the large proportion of  $TG_{ERR}$  attributable to  $ENT_{ERR}$ . Therefore, predictors of  $ENT_{ERR}$  were also examined. The  $ENT_{ERR}$  is characterized by a high degree of random variability, but GLM confirmed that the implantation angle is a weak but significant predictor ( $p < 0.001$ ) in the model:  $ENT_{ERR} = 2.75 - 0.015 \cdot (90^\circ - \alpha)$  (estimated dispersion of  $1$  mm, F-statistic vs. constant model of  $12.5$ ,  $p < 0.001$ ). In other words, every  $10^\circ$  of deviation from the

ideal (perpendicular) implantation angle increased the entry point error by  $0.15$  mm (Fig. 7C).

Substitution of the average parameter values (Table I) into the  $TG_{ERR}$ -model illustrates the roles of individual components in the average accuracy  $TG_{ERR} = 2.4$  mm (100%). The average entry point error accounted for  $0.54 \cdot 1.7 = 0.92$  mm (38%), the increase in trajectory deflection with depth accounted for  $0.31 \cdot 43.4 \cdot \tan(1.8) = 0.42$  mm (18%), and the insertion depth error accounted for  $0.09 \cdot 0.5 = 0.05$  mm (2%). Together, they account for  $1.39$  mm of error (58%). The remaining  $1$  mm (42%) is attributable to random variance.

## IV. DISCUSSION

### A. Contacts localization

Long-term invasive recording using SEEG electrodes enables the acquisition of brain signals to define the epileptogenic zone and allow precise surgical resection planning in the context of individual patient brain anatomy. Therefore, accurate anatomical localization of implanted electrode contacts is crucial to identifying epileptiform activity, interpreting stimulation mapping of the eloquent cortex, and performing radio-frequency thermocoagulation at selected contacts.

Although many useful assistive labeling software tools and approaches exist to reduce the time required for manual labeling, their robustness and reliability in detecting individual contacts are limited [18]–[22]. The limitations of previously developed methods lie pertain to identification of individual contacts subsequently grouped to an electrode, which principally fails in nearby, crossing, or touching electrodes. X-ray

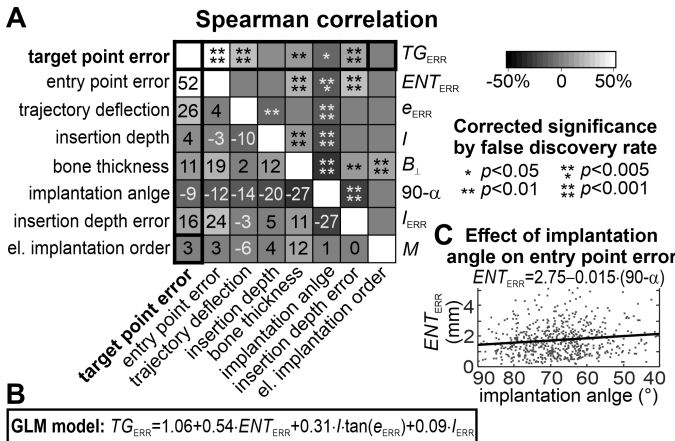


**Fig. 7.** Multifactorial analysis of factors influencing target point error. (A) Spearman correlation demonstrates dependency on entry point error  $ENT_{ERR}$ , less on trajectory deflection  $e_{ERR}$ , and less on insertion depth error  $I_{ERR}$ . (B) Generalized linear model (GLM) reveals dependency on insertion depth  $I$ , which is multiplied by the trajectory deflection, and insertion depth error. (C)  $ENT_{ERR}$  was slightly worse for smaller implantation angles.

artifacts often distort contact intensity and make the shape of a contact difficult to detect. Contacts not used for recording often lie within the anchor bolt, and a known number of contacts at the electrode cannot be viewed in CT. Detection algorithms that search a fixed number of contacts therefore fail. The precision of localization in a voxel raster is limited mainly in low-resolution images. Similarly, electrode approximation using a linear function is helpful for visual inspection but insufficient for precise measurement.

Our approach inverts the whole process. Entire electrodes were identified to approximate them by polynomial curves in a 3D space. A curvilinear electrode model makes it possible to find all (even indistinct) contacts at once with precise positioning under voxel resolution in low-quality slices; e.g., planar electrode placement in the plane of scanning causes smoothing and merging of contacts. This approach has no false detection problem and is significantly more sensitive and specific than previously published algorithms, including ones with a >10% error rate [19], 6% [20], and >5% [21] false positive rates. The labels' precision was also significantly better than that achieved with the tool used for semi-automated manual labeling considered to be the gold standard [22]. Only one disputable failure was registered for crossing and touching electrode placement, where the first contact was difficult to identify and label manually. This led to shifting contact orders by one.

Metal implants in head volumes (shunts, clips, amalgam seals) could potentially limit fully automated detection if automated metal subtraction from pre-implantation CT fails. Additional masking could be done manually that would potentially slightly prolong image pre-processing. The second limitation of the algorithm is the requirement to know the electrode trajectory for the GMM algorithm initialization, which is difficult or impossible to obtain in frameless systems. However, this can be easily resolved: the planned electrode trajectory can be replaced by two-point coordinates manually

placed close to the tip and entry point, without restrictions on the label precision. The voxel-based masking of metals and point fiducial placements is achieved with 3D Slicer and other tools.

Although the algorithm developed in this study is intended for use in measuring and parametrizing implantation trajectories, the detector itself was proven to be highly capable in automated/semi-automated electrode labeling (available at website [github.com/EpiReC-ISARG](https://github.com/EpiReC-ISARG)). The list of contact coordinates in RAS can be transformed to MNI (Montreal Neurological Institute-Hospital) space and used for anatomical localization of structures in atlases.

## B. Measurement of electrode placement

Assessment of electrode placement accuracy is not new. However, previously published studies focused predominantly on target point error [17], [29]–[33] and only rarely examined entry point error [23], [34], [35]. All of these previous studies relied on manual labeling of approximate localization of electrode tips for comparison with planned targets in CT/MRI scans. Complex descriptions of the electrode trajectory, angular deviation from the planned trajectories, and the relationship of each to the skull were not provided. In this study, we implemented automated measurement of all implantation parameters: tip localization, entry point (extracranial and intracranial), deviation of contacts from the central axis, minimal distances of first contacts from the trajectory, implantation depth, bone thickness at the anchor bolt, implantation angle with respect to the skull, and deviation from the planned trajectory.

Not all measured parameters were validated visually for all 662 electrodes (8,745 contacts). However, the outlying cases were confirmed manually using 3D Slicer.

The bone stabilizes the anchor bolt and establishes the insertion trajectory. The minimal recommended bone thickness is 2 mm for screwing, but this issue has only rarely been examined [23]. We demonstrated the average cranial thickness over a 3D skull model that confirmed the physical measurement [36]. Similarly, assessment of the implantation angle to the spherical skull surface has been studied only sporadically [23], [24]. Manual measurement in orthogonal plane projections can be misleading. Although the surgeon checked planned implantation angles that exceeded 60°, accurate measurement in 3D revealed that almost 1/5 of the electrodes were under this limit. Our novel automated image measurement of the bone thickness and implantation angle allows for early identification (before surgery) of planned trajectories that are outside the recommended ranges.

## C. Effects influencing implantation accuracy

Although the primary goal of the work was to develop an automated system for identifying and measuring electrode parameters, its retrospective application yielded clinically relevant feedback for our epilepsy surgery program. Our experiences could possibly be extrapolated to other centers employing the SEEG technique. Detailed analysis revealed the weaknesses of the frame-based stereotaxy and could help to

minimize them. The representative parameter of the total accuracy is the target point error ( $TG_{ERR}$ ), which varies slightly depending on the implantation approach (non-robot/robot assistant, type of frame stereotaxy, preference of orthogonal or oblique trajectories, team experience). Retrospective reviews have demonstrated  $TG_{ERR}$  ranging from 1.5 to 2.9 mm [17], [23], [34], [35]. The average  $TG_{ERR} = 2.4$  mm observed in our study is equal to that of a frame non-robotic or frameless robotic assistant system [17]. However, the inclusion of deformed electrodes decreased the average accuracy to 2.65 mm, which was slightly better than that obtained in methodologically similar work [23]. As the experience of our surgical team increased, the accuracy increased by 0.12 mm per year (or 100 electrodes), which is similar to that observed in previous work [32].

Regardless of whether the stereotactic implantation of deep electrodes is performed with or without a frame and with or without a robot, it is essential to achieve the highest possible implantation accuracy [16], [17]. Implantation accuracy studies focused specifically on the Cosman–Robert–Wells system (CRW) were found only for deep brain stimulation (DBS), for which CRW represents a small proportion (<10%) of technique usage [17], [29]. Thus, to the best of our knowledge, this is the first study to evaluate the accuracy of the CRW for SEEG. The  $TG_{ERR}$  of DBS using CRW was usually better < 2 mm [30]–[33], [37]. However, the implantation accuracy of DBS is superior to SEEG in general [17] because it is a more routine procedure without anchor bolt drilling.

Although angular electrode deflection from the planned trajectory is logically considered to be a reason for the target error increasing with insertion depth [29], [32], objective validation of this is rare. Therefore, the measured trajectory deflection was also used as a testing factor to predict the target accuracy. Multifactorial analyses of objectively measured parameters revealed the crucial effect of the entry point accuracy, which accounted for 38% of the total error. A shift in the entry point caused only a small angle deviation in the CRW system, which increased with implantation depth and accounted for 18% of the total error, as in [23]. The implantation trajectory accuracy was represented by the minimal distance of the electrode tip from the planned trajectory, which was approximately 10% less than the total target point error. A minor effect of implantation depth on the target point error (2%) is consistent with a previous comparison of insular (depth  $66 \pm 11$  mm) and non-insular (depth  $28 \pm 9$  mm) electrodes [34]. This finding confirms the greater accuracy of the more expensive robot-assistant frame system, which fixes the entry point more stably [17]. The remaining 42% of the error could not be fully explained and probably represented random error. We conclude that stabilizing the entry point can help to minimize  $TG_{ERR}$  in the first step.

A surprising result was the minimal effect of the electrode implantation angle on  $TG_{ERR}$ , also reported in [23]. The GLM excluded implantation angle as a significant direct predictor of  $TG_{ERR}$ . However, a smaller implantation angle worsens the entry point error and thus can indirectly affect the target point. Therefore, our results support the premise that low-angle drilling probably causes the drill bit to slip and indirectly

decreases accuracy, but to a much lesser extent than expected. Cranial thickness was not found to be correlated with implantation errors either, and the stability of anchor bolt placement was similar for thin (cortical tissue) and strong (cortical and spongy tissue) bone.

The last excluded effect was error progression over time during surgery: precision was not affected by the drilling order of electrode entries. The effect of cerebrospinal fluid leakage on electrode placement is minimal because electrode insertion typically occurs at the end of surgery, long after drilling and anchor bolt screwing. Evaluation of the achievement of target brain structures [38] was not tested in this study.

The reasons for inaccurate implantation of SEEG electrodes, including detailed analysis of the causes of their inaccuracy, remain to be studied. The methodology presented in this study allows for robust parameterization of SEEG electrode placement for multifactorial objective validation. A future study's task will be to eliminate random and human/technical factors that lead to failures of the implantation system. An additional intraoperative control system should be developed to detect hidden stereotactic frame displacement. On average, the unpredictable electrode deformation mentioned in previous studies [23], [35] was observed at every 29<sup>th</sup> electrode (3.4%) when the electrode trajectory changed in subdural space or sulcus (from gyrus to gyrus). Therefore, detailed studies of anatomical factors that cause implantation failures need to be performed in the future.

## V. CONCLUSION

We designed and validated a robust algorithm for automated detection and precise labeling of all SEEG electrode contacts in CT scans. A retrospective comparison of planned vs. implanted electrode placement demonstrated implantation accuracy consistent with that reported in previous studies. Six hundred electrode trajectories and interrelations with the skull were measured and analyzed to identify the factors that influence implantation accuracy. A multifactorial analysis revealed significant causes of inaccuracy to be entry point error (38%), angular trajectory deflection (18%), insertion depth error (2%), and random error (42%). The proposed method will contribute to safer electrode implantation, increase intracranial recording yield, and facilitate future research requiring precise anatomical localization of contacts.

## ACKNOWLEDGMENT

Thanks CESNET for access to datastorage facility. Special thanks Jan Jirasek for provided technical information from Cardion Ltd, distributor of Cosman-Robert-Wells system and Dixi Médical SEEG accessories in Czech Republic.

## REFERENCES

- [1] P. Ryvlin, J. H. Cross, and S. Rheims, "Epilepsy surgery in children and adults," *Lancet. Neurol.*, vol. 13, no. 11, pp. 1114–1126, Nov. 2014, doi: 10.1016/S1474-4422(14)70156-5.
- [2] S. Wiebe, W. T. Blume, J. P. Girvin, and M. Eliasziw, "A Randomized, Controlled Trial of Surgery for Temporal-Lobe Epilepsy," *N. Engl. J. Med.*, vol. 345, no. 5, pp. 311–318, Aug. 2001, doi: 10.1056/nejm200108023450501.

- [3] I. Blumcke et al., "Histopathological findings in brain tissue obtained during epilepsy surgery," *N. Engl. J. Med.*, vol. 377, no. 17, pp. 1648–1656, Oct. 2017, doi: 10.1056/NEJMoa1703784.
- [4] F. Rosenow and H. Lüders, "Presurgical evaluation of epilepsy," *Brain*, vol. 124, no. 9, pp. 1683–1700, Sep. 2001, doi: 10.1093/BRAIN/124.9.1683.
- [5] P. Krsek et al., "Incomplete resection of focal cortical dysplasia is the main predictor of poor postoperative outcome," *Neurology*, vol. 72, no. 3, pp. 217–223, Jan. 2009, doi: 10.1212/01.WNL.0000334365.22854.D3.
- [6] I. S. Fernández and T. Lodenkemper, "Electrocorticography for seizure foci mapping in epilepsy surgery," *J. Clin. Neurophysiol.*, vol. 30, no. 6, pp. 554–570, Dec. 2013, doi: 10.1097/01.WNP.0000436898.10125.70.
- [7] C. Rathore and K. Radhakrishnan, "Concept of epilepsy surgery and presurgical evaluation," *Epileptic Disord.*, vol. 17, no. 1, pp. 19–31, Mar. 2015, doi: 10.1684/EPD.2014.0720.
- [8] F. Bartolomei et al., "Defining epileptogenic networks: Contribution of SEEG and signal analysis," *Epilepsia*, vol. 58, no. 7, pp. 1131–1147, Jul. 2017, doi: 10.1111/epi.13791.
- [9] H. Joswig et al., "Stereoelectroencephalography Versus Subdural Strip Electrode Implants: Feasibility, Complications, and Outcomes in 500 Intracranial Monitoring Cases for Drug-Resistant Epilepsy," *Neurosurgery*, vol. 87, no. 1, pp. E23–E30, Jul. 2020, doi: 10.1093/NEUROS/NYAA112.
- [10] N. Tandon et al., "Analysis of Morbidity and Outcomes Associated With Use of Subdural Grids vs Stereoelectroencephalography in Patients With Intractable Epilepsy," *JAMA Neurol.*, vol. 76, no. 6, pp. 672–681, Jun. 2019, doi: 10.1001/JAMANEUROL.2019.0098.
- [11] M. Toth et al., "Surgical outcomes related to invasive EEG monitoring with subdural grids or depth electrodes in adults: A systematic review and meta-analysis," *Seizure*, vol. 70, pp. 12–19, Aug. 2019, doi: 10.1016/j.SEIZURE.2019.06.022.
- [12] M. O. Baud et al., "European trends in epilepsy surgery," *Neurology*, vol. 91, no. 2, pp. e96–e106, Jul. 2018, doi: 10.1212/WNL.0000000000005776.
- [13] H. J. Lamberink, K. Boshuisen, P. C. Van Rijen, P. H. Gosselaar, and K. P. J. Braun, "Changing profiles of pediatric epilepsy surgery candidates over time: A nationwide single-center experience from 1990 to 2011," *Epilepsia*, vol. 56, no. 5, pp. 717–725, May 2015, doi: 10.1111/EPI.12974.
- [14] F. Cardinale, G. Casaceli, F. Ranieri, J. Miller, and G. Lo Russo, "Implantation of Stereoelectroencephalography Electrodes: A Systematic Review," *J. Clin. Neurophysiol.*, vol. 33, no. 6, Lippincott Williams and Wilkins, pp. 490–502, Dec. 01, 2016, doi: 10.1097/WNP.0000000000000249.
- [15] J. Gonzalez-Martinez, J. Bulacio, A. Alexopoulos, L. Jehi, W. Bingaman, and I. Najm, "Stereoelectroencephalography in the 'difficult to localize' refractory focal epilepsy: Early experience from a North American epilepsy center," *Epilepsia*, vol. 54, no. 2, pp. 323–330, Feb. 2013, doi: 10.1111/j.1528-1167.2012.03672.x.
- [16] V. N. Vakharia et al., "Accuracy of intracranial electrode placement for stereoelectrocephalography: A systematic review and meta-analysis," *Epilepsia*, vol. 58, no. 6, pp. 921–932, Jun. 2017, doi: 10.1111/EPI.13713.
- [17] L. R. Philipp, C. M. Matias, S. Thalheimer, S. H. Mehta, A. Sharan, and C. Wu, "Robot-Assisted Stereotaxy Reduces Target Error: A Meta-Analysis and Meta-Regression of 6056 Trajectories," *Neurosurgery*, vol. 88, no. 2, pp. 222–233, Oct. 2021, doi: 10.1093/neurology/nyaa428.
- [18] B. Ervin et al., "Fast Automated Stereo-EEG Electrode Contact Identification and Labeling Ensemble," *Stereotact. Funct. Neurosurg.*, vol. 99, no. 5, pp. 393–404, Aug. 2021, doi: 10.1159/000515090.
- [19] M. Narizzano et al., "SEEG assistant: A 3DSlicer extension to support epilepsy surgery," *BMC Bioinformatics*, vol. 18, no. 1, pp. 1–13, Feb. 2017, doi: 10.1186/S12859-017-1545-8/FIGURES/6.
- [20] A. Granados et al., "Automatic segmentation of stereoelectroencephalography (SEEG) electrodes post-implantation considering bending," *Int. J. Comput. Assist. Radiol. Surg.*, vol. 13, no. 6, pp. 935–946, Jun. 2018, doi: 10.1007/s11548-018-1740-8.
- [21] S. Medina Villalon et al., "EpiTools, A software suite for presurgical brain mapping in epilepsy: Intracerebral EEG," *J. Neurosci. Methods*, vol. 303, pp. 7–15, Jun. 2018, doi: 10.1016/j.jneumeth.2018.03.018.
- [22] A. Joshi et al., "Unified framework for development, deployment and robust testing of neuroimaging algorithms," *Neuroinformatics*, vol. 9, no. 1, pp. 69–84, Mar. 2011, doi: 10.1007/s12021-010-0902-8.
- [23] L. E. van der Loo et al., "Methodology, outcome, safety and in vivo accuracy in traditional frame-based stereoelectroencephalography," *Acta Neurochir. (Wien)*, vol. 159, no. 9, pp. 1733–1746, Sep. 2017, doi: 10.1007/s00701-017-3242-9.
- [24] J. C. Iordanou, D. Camara, S. Ghatan, and F. Panov, "Approach Angle Affects Accuracy in Robotic Stereoelectroencephalography Lead Placement," *World Neurosurg.*, vol. 128, pp. e322–e328, Aug. 2019, doi: 10.1016/j.wneu.2019.04.143.
- [25] "3D Slicer image computing platform — 3D Slicer," 2021. <https://www.slicer.org/> (accessed Dec. 10, 2021).
- [26] "SPM12 Software - Statistical Parametric Mapping." <https://www.fil.ion.ucl.ac.uk/spm/software/spm12/> (accessed Dec. 10, 2021).
- [27] W. Penny, K. Friston, J. Ashburner, S. Kiebel, and T. Nichols, *Statistical Parametric Mapping: The Analysis of Functional Brain Images*. Elsevier Ltd. 2007.
- [28] L. M. Willems et al., "Invasive EEG-electrodes in presurgical evaluation of epilepsies: Systematic analysis of implantation-, video-EEG-monitoring- and explantation-related complications, and review of literature," *Epilepsy Behav.*, vol. 91, pp. 30–37, Feb. 2019, doi: 10.1016/j.yebeh.2018.05.012.
- [29] Z. Li, J. G. Zhang, Y. Ye, and X. Li, "Review on Factors Affecting Targeting Accuracy of Deep Brain Stimulation Electrode Implantation between 2001 and 2015," *Stereotact. Funct. Neurosurg.*, vol. 94, no. 6, pp. 351–362, Jan. 2016, doi: 10.1159/000449206.
- [30] F. Duffner, H. Schiffbauer, S. Breit, S. Friese, and D. Freudenstein, "Relevance of Image Fusion for Target Point Determination in Functional Neurosurgery," *Acta Neurochir.* 2002 1445, vol. 144, no. 5, pp. 445–451, 2002, doi: 10.1007/S007010200065.
- [31] C. Pollo et al., "Localization of electrodes in the subthalamic nucleus on magnetic resonance imaging," *J. Neurosurg.*, vol. 106, no. 1, pp. 36–44, 2007, doi: 10.3171/jns.2007.106.1.36.
- [32] C. Kelman, V. Ramakrishnan, A. Davies, and K. Holloway, "Analysis of stereotactic accuracy of the cosman-robert-wells frame and nexframe frameless systems in deep brain stimulation surgery," *Stereotact. Funct. Neurosurg.*, vol. 88, no. 5, pp. 288–295, Sep. 2010, doi: 10.1159/000316761.
- [33] M. J. Katati et al., "An initial experience with intraoperative O-Arm for deep brain stimulation surgery: can it replace post-operative MRI?," *Acta Neurol. Belg.*, vol. 120, no. 2, pp. 295–301, Apr. 2020, doi: 10.1007/S13760-018-1037-2/TABLES/2.
- [34] K. Machetanz et al., "Frame-based and robot-assisted insular stereoelectroencephalography via an anterior or posterior oblique approach," *J. Neurosurg.*, vol. 1, no. aop, pp. 1–10, Apr. 2021, doi: 10.3171/2020.10.JNS201843.
- [35] F. Cardinale et al., "Stereoelectroencephalography: surgical methodology, safety, and stereotactic application accuracy in 500 procedures," *Neurosurgery*, vol. 72, no. 3, pp. 353–366, Mar. 2013, doi: 10.1227/NEU.0B013E31827D1161.
- [36] I. Del Olmo Llanes, E. Bruner, O. Cambra-Moo, M. Molina Moreno, and A. González Martín, "Cranial vault thickness measurement and distribution: a study with a magnetic calliper," *Anthropol. Sci.*, vol. 127, no. 1, pp. 47–54, 2019, doi: 10.1537/ASE.190306.
- [37] J. D. Carlson, K. E. McLeod, P. S. McLeod, and J. B. Mark, "Stereotactic accuracy and surgical utility of the O-arm in deep brain stimulation surgery," *Oper. Neurosurg.*, vol. 13, no. 1, pp. 96–107, Feb. 2017, doi: 10.1227/NEU.0000000000001326.
- [38] P. Bourdillon et al., "Effective accuracy of stereoelectroencephalography: Robotic 3D versus Talairach orthogonal approaches," *J. Neurosurg.*, vol. 131, no. 6, pp. 1938–1946, Dec. 2019, doi: 10.3171/2018.7.JNS181164.